Version of Record: https://www.sciencedirect.com/science/article/pii/S0927025620303840
Manuscript_073b0f9d8d366182369dc8e2a1947e84

Migration Energy Barriers and Diffusion Anisotropy of Point Defects on Tungsten Surfaces

Jiannan Hao[1,2,3,4, †], Shuo Jin[1,2], Guang-Hong Lu[1,2, *], Haixuan Xu[3,4, *]

[1]*School of Physics, Beihang University, Beijing 100191, China*

[2]*Beijing Key Laboratory of Advanced Nuclear Materials and Physics, Beihang University, Beijing 100191, China*

[3]*Department of Materials Science and Engineering, University of Tennessee, Knoxville, Tennessee 37996, USA*

[4]*Joint Institute for Advanced Materials, Knoxville, Tennessee 37996, USA*

Abstract

Tungsten is one of the most promising candidates for plasma-facing materials in future fusion devices, owing to its high performance under extreme irradiation conditions. However, irradiation-induced surface morphology varies significantly, depending on the irradiation type, fluence, and flux. Therefore, it is critical to examine the dynamics of point defects on tungsten (W) surfaces to understand how irradiation affects surface morphology. In this study, we employ the Self-Evolving Atomistic Kinetic Monte Carlo (SEAKMC) method to search for potential migration paths of point defects on W (100), (110) and (111) surfaces. The first-principles calculations are then used to accurately determine the migration energy barriers. The obtained paths and barriers are incorporated into a kinetic Monte Carlo (KMC) model to determine trajectories and diffusivities, which are described by diffusion tensors to demonstrate their anisotropic features. Multiple diffusion mechanisms have been identified on different surfaces, with various anisotropy factors. Particularly, point defects on the W (110) surface have the highest diffusivities, with anisotropy factors independent of temperatures. In comparison, the anisotropy of the W (100) surface decreases as temperature increases, while the W (111) surface is isotropic for point defects. This study provides insights into defect transport properties on different surfaces, which are essential for understanding the early stages of irradiation-induced microstructural evolutions and surface morphology of tungsten.

Keywords: tungsten, diffusion, anisotropy, surface, on-the-fly kinetic Monte Carlo

© 2020 published by Elsevier. This manuscript is made available under the Elsevier user license
https://www.elsevier.com/open-access/userlicense/1.0/

† Visiting student at UTK

*Corresponding author

Guang-Hong Lu: lgh@buaa.edu.cn

Haixuan Xu: xhx@utk.edu

I. INTRODUCTION

Tungsten (W) is considered one of the most promising candidates for plasma-facing material in future fusion devices, owing to its high melting point, high thermal conductivity, high sputtering threshold, and low hydrogen retention [1-3]. However, the interaction between plasma and tungsten surfaces can significantly influence the thermal and mechanical properties and performances of the material. [4-9]. Previous studies have shown that surface morphology of blisters of tungsten depends on both the plasma fluence and surface directions [10-12]. For instance, triangular and sponge-like structures were found on <111> and <100> grain surfaces, respectively, and in other directions with lamellae structures [10]. There are significant dependencies of surface orientations after helium plasma irradiation [13,14]. On the contrary, the growth of fuzz-like microstructures was found to have no orientational preference as reported by Parish et al. [15]. The contributing factors to morphology changes include the creation of vast numbers of point defects, the diffusion of radiation-induced point defects [16], and their migration to surfaces during the sputtering and deposition by energetic ions [17-19]. However, the underlying mechanisms that lead to different morphologies and microstructures remain unclear, particularly the dependence of surface orientations. Therefore, to understand the formation mechanisms of different surface patterns, it is essential to reveal the effects of point defect migration on tungsten surfaces.

The self-diffusion of a tungsten adatom at certain low-index planes has been observed experimentally [20-23] and studied theoretically [23-29]. Using a field ion microscope, Senft et al. found one-dimensional (1D) diffusion of adatoms on the W(211) surface [23]; the diffusivities of adatoms on the W(110) and W(211) surface were given by Antczak et al. [30,31]. Chen et al. studied adatom migration on the W(100) and (110) surfaces using first-principles calculations [27], where the surface crowdion migration mechanisms were investigated. D. Chen et al. found the self-diffusion processes of adatom clusters on the W(110) surface rely on a successive hopping mechanism using molecular dynamics (MD) [25]. Furthermore, Jansson et al. investigated diffusion mechanisms of an adatom on the W(100), (110), and (111) surfaces using interatomic potentials in combination with kinetic Monte Carlo (KMC) [32]. However, only a few works of vacancy migration on tungsten surfaces have been carried out. Wen et al. [33] reported that a vacancy is easier to form and migrate on the W(001) surface than in bulk using interatomic potential, and Duan et al. [34] focused on the

vacancy cluster behaviors toward the W(001) surface using molecular statics in combination with KMC. The interatomic potentials used in the previous works were not fitted from the properties of surface defects, and the migration mechanisms of surface defects are artificially guessed and chosen in the simulations. It is known that certain tungsten surfaces may reconstruct and that reconstruction introduces the anisotropy of point defects by intrinsically rearranging the atoms on surfaces. For instance, the reconstructed W(100) surface was observed experimentally [35], and it was found that under 400 K, a $c(2 \times 2)$ structure could exist without impurities [36]. In addition, impurities could easily lead to surface reconstruction, e.g., hydrogen [37-39] or sulfur [40], which is an inevitable factor under plasma irradiation. However, the migration mechanisms and barriers of adatoms on W(100) and (110) given by Chen et al. [27] were calculated on perfect surfaces without reconstruction. Olewicz et al. [41] further considered reconstructed W(100) surface by DFT and correlated the DFT results with experimental observations using a filed ion microscope at 650-700 K. To the best of our knowledge, although several studies did consider anisotropic diffusion on tungsten surfaces by differentiating the diffusivities along different coordinate axes [42,43], they did not investigate the directional correlation of diffusivities (based on diffusion tensor [44]), resulting in the loss of information about the correlation of different directions and the temperature dependence of anisotropy, which is essential for the understanding of the orientation-dependent evolution of surface defects.

This work focuses primarily on the single adatom and vacancy migration on the low-index surfaces of W, which are the (110), (111), and (100) surfaces representing 2-, 3-, and 4-fold rotational symmetries, respectively. Particularly, the reconstructed (100) surface is examined and compared with the non-reconstructed (100) surface produced by different interatomic potentials. In addition, the (100) and (111) surfaces are chosen because they are the most and least resistant surfaces to hydrogen blister formation, respectively [12]. In contrast, the (110) surface is chosen due to its close-pack structure and the lowest surface energy among the low-index surfaces [45,46]. The migration mechanisms are predicted by the Self-Evolving Atomistic Kinetic Monte Carlo (SEAKMC) [47-49] method coupled with interatomic potentials. The identified paths are checked with the nudged elastic band (NEB) method [50-53]. Then, the migration energy barriers (MEBs) of each mechanism or path are quantified using density functional theory (DFT) calculations. All of this information is incorporated into a KMC model to obtain the diffusivities and diffusion tensors at different

temperatures. This paper is organized as follows: Sect. II is a brief introduction of the computational methodology used in calculations; Sect. III details results and discusses adatom and vacancy migration paths and diffusivities on W (100), (110) and (111) surfaces; and Sect. IV is the summary.

II. METHODOLOGY AND SIMULATION DETAILS

A. Interatomic Potentials

Three interatomic potentials for tungsten are employed and compared in this work. Particularly, we examined (i) a Finnis-Sinclair potential [54] initially developed by Ackland and Thetford [55] and modified at short range by Juslin and Wirth [56] (POT_J); (ii) a Tersoff-type [57] bond-order potential (BOP) for W-H-He developed by Li et al.[58,59] (POT_L); and (iii) a recently developed embedded atom model [60] (EAM) potential for W-H and defects by Wang et al. [61], in which the W-W interaction is derived from Marinica et al. [62] (POT_M).

A summary of the fundamental properties of point defects calculated using these potentials, both in bulk and on the surfaces, is given in **Table 1**, which compares defect formation energies, migration energies, and surface energies. The migration mechanisms of point defects and corresponding MEB trends yielded by these interatomic potentials are consistent with our DFT results and other's works [27,40,41,63,64]. However, it should be noted that none of the potentials are specifically fitted to surface properties, limiting their applications for simulations of multiple defects with defect interaction on different surfaces. The stable sites of defects on three surfaces with their neighbor sites are illustrated in **Fig. 1**, which shows that the same position is preferred by both an adatom and a vacancy.

Table 1. Fundamental properties of the bulk, three surfaces, and point defects using interatomic potentials and DFT, compared to the experimental results and works of others ([a] [65], [b] [66], [c] [67], [d] [68], [e] [69], [f] [45], [g] [70], [h] [63], [i] [71], [j] [72], [k] [73], [l] [40], [m] [74], [n] [64] and [o] [58])**.** The Δγ (100) and Δγ (111) represent the difference in surface energy compared to γ (110). The Δγ of DFT is calculated from the original surface energy in reference [42]. Data in column POT_J, POT_M and POT_L are obtained from their initial papers [56,59,62], respectively. All energies of SFP are calculated in this work. (Notes: * = data recalculated in this work; $_{f}$ = formation energy; $_{mig}$ = migration energy; $_{rot}$ = rotation energy; SIA = self-interstitial atom; V=vacancy; NN=nearest neighbor; all energies are in eV.)

	Experiments	DFT	POT_J	POT_M	POT_L
α (bcc) (Å)	3.165 [a, b]	3.174 [c]	3.1652	3.14	3.165
E_c (bcc)	-8.90 [a]	-8.59 [c]	-8.9	-8.9	-8.906
γ (110) (J/m^2)	3.265 [d], 3.675 [d]	4.005 [f]	2.576 [*]	2.306 [*]	2.319 [*]
Δγ (100) (J/m^2)		0.630 [f]	0.348 [*]	0.415 [*]	0.838 [*]
Δγ (111) (J/m^2)		0.447 [f]	0.726 [*]	0.657 [*]	0.903 [*]
$E_f^{SIA<111>}$	9.06±0.63 [g]	9.86 [h]	9.50	10.52	9.33
E_f^V	3.68±0.2 [i], 3.6 [j]	3.34 [h]	3.63 [*]	3.49	3.52
$E_{mig}^{SIA<111>}$	0.054±0.005 [k]	0.005 [h], 0.052 [l]	0.007 [*]	0.020 [*]	0.006 [*]
$E_{rot}^{SIA<111>}$		0.35 [l]	0.670 [*]	0.459 [*]	0.251 [*]
$E_{mig}^{V(1NN)}$	1.68±0.06 [m],	1.5 [l], 1.78 [n]	1.451 [*]	1.856 [*]	1.813 [*]
$E_{mig}^{V(2NN)}$	1.78±0.1 [i]	5.54 [n]	5.304 [*]	7.507 [*]	6.821 [*]

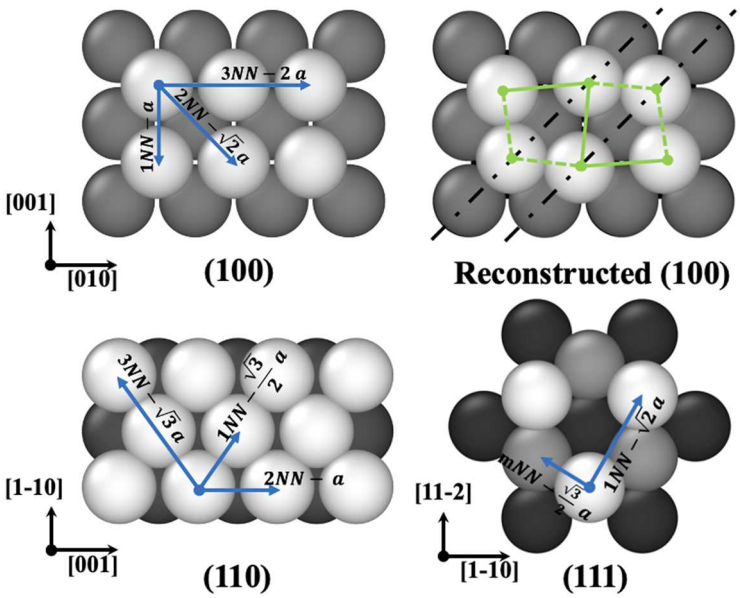

Fig. 1. Top view of the nearest neighbor sites of point defects on the perfect W (100), (110), (111), and the reconstructed (100) surface. The gray-scaled spheres (from white to black) represent the depths of atoms in each orientation. The arrows denote the direction and distance of different neighbor sites, where and *x*NN represents the xth nearest neighbor site and a is the lattice constant. For the reconstructed (100) surface, the green solid and dashed lines linking the atoms are designated as long bridge and short bridge [75], respectively, where the atoms and bridges are symmetric about the mirror axes (dash-dot lines). On the W (111) surface, a metastable state, denoted mNN, is located at the second layer, so the arrow between the first and second layers represents a projection of the real distance onto the (111) plane. All positions and atomistic displacements are directly from DFT configurations.

B. Identifying Potential Migration Paths of Point Defects

The migration paths of point defects on the tungsten surfaces are initially obtained using the SEAKMC code developed by Xu et al. [47-49]. Xu et al. developed a selective active volume (AV) scheme using the dimer method [76,77] to locally search the transition state of the defects of interest in the system to identify any potential saddle points, which accelerates the identification of new events during defects dynamics. The saddle point search is carried out over 2000 times for each defect on every surface to identify the possible mechanisms. After initially guessing the migration path from

SEAKMC, we employ the NEB method [50-53], built in the LAMMPS code [78], as a supplemental verification of the mechanisms. POT_J and POT_M are implemented in the SEAKMC code, and all three potentials (in Sect. II. A) are used in LAMMPS.

For the saddle point searches using the SEAKMC, the AV size ranges from 2.2 to 3.7 lattice constants for point defects on surfaces. A minimum length of 15 Å vacuum space is added between the slabs, depending on the surface directions, to avoid any surface-surface interactions. The atoms at the bottom of the boxes are fixed to mimic the bulk properties.

C. Determining Migration Energy Barriers using First-Principles Calculations

First-principles DFT is used to accurately determine the MEBs for each of the migration paths identified by the three interatomic potentials. In particular, the generalized gradient approximation (GGA) [79], implemented in the Vienna Ab-initio Simulation Package (VASP) code [80-82] and the NEB with climbing image modification [50] are employed to calculate the MEBs. As before, a vacuum length of 15 Å along the surface direction is inserted between each slab to avoid image interaction under periodic boundary conditions in DFT calculation. The supercell for the (100) surface is an orthogonal box of $12.7 \times 12.7 \times (12.7 + 15)$ $Å^3$, including 8 layers (128 atoms) of atoms with the bottom 3 layers fixed. For the reconstructed (100) surface, the top layer of atoms is rearranged (see **Fig. 1**), consistent with the results by Debe et al. [35], and the reconstructed W{100} surfaces display a p2mg symmetry at < 190 K and would degenerate to the perfect (100) surface structure above 400 K [83]. The size of (110) supercell is as $12.7 \times 13.5 \times (13.5 + 15)$ $Å^3$, containing 6 layers of atoms (144 atoms) with the bottom 3 layers fixed. The size of (111) surface slab is $15.5 \times 13.5 \times (16.5 + 15)$ $Å^3$, containing 18 layers of atoms (216 atoms) with the bottom 8 layers fixed. The lattice spacings for the three surfaces are illustrated in **Fig. 1**. The cutoff energy is set to be 500 eV and a $4 \times 4 \times 1$ k-points by Monkhorst–Pack scheme [84] is applied to the slab models of all three surfaces. The optimization of stable and transition states stops when the forces on all the atoms are less than 10^{-3} and 10^{-2} eV/Å, respectively.

D. Kinetic Monte Carlo

The KMC method is used to generate the trajectories of point defects on the surfaces with the obtained MEBs from DFT including all identified diffusion mechanisms, where several mechanisms

in SEAKMC or reported by previous work [27] are excluded due to high MEBs or extreme low possibilities of occurrence, e.g., non-first-nearest neighbor jumps. In this work, we consider only single point defects on surfaces, assuming no interactions between point defects, and apply two-dimensional (2D) periodic boundary conditions. The rate of a defect jumping from one site to another based on the harmonic transition state theory [85-87] is given by,

$$R_i = \nu_i \cdot \mathrm{e}^{-\frac{E_i}{k_B T}} , \quad (1)$$

where ν_i is the attempt frequency of defects, E_i is the migration energy, and k_B and T are the Boltzmann constant and temperature, respectively. The attempt frequency ν_i is set to be $10^{12}\ s^{-1}$ for all cases as a constant in KMC calculations. The lattice constants of all surfaces are set to be 3.165 Å [65,66] in KMC simulations, independent of potentials. The timestep dt is calculated by the residence-time algorithm [88]. To obtain the diffusivities of an adatom or a vacancy on the three surfaces, we carry out 10 simulations for each type of defects on the three surfaces, each simulation containing 10000 trajectories of point defects at temperatures ranging from 100 to 1500 K with a 100 K interval. The simulations stop when the total steps reach 1 million for each case. [cite PRB]

E. Diffusivity and Diffusion Tensor

The diffusivity, given by the Fick's laws, is generally considered as a scalar in most isotropic diffusion processes and can be derived from mean square displacement (MSD) from the Brownian motion. However, for particle or defect migration in anisotropic materials, e.g., diffusion on surfaces of metals [44,89], diffusivity can be described as a second-rank tensor $\boldsymbol{D}$ (D_{ij}) [90]. In terms of a 2D system, D'_{xx} and D'_{yy} are the diagonal components of the diagonalized diffusion tensor, or the eigenvalues of $\boldsymbol{D}$, also known as the principal values associated with eigenvectors (Fig. 2). The 1D diffusivity from any observation direction can be expressed by the direction cosines [90]. Along with a rotation matrix, we can write the diffusivity as a function of the observation direction,

$$D(\theta) = \overline{D} + \overline{D} \cdot e \cdot \cos\big(2(\theta - \phi)\big), \quad (2)$$

where $\overline{D}$ is the integral average of $D(\theta)$. Here, we define the anisotropy factor e at a certain temperature,

$$e = \frac{D_{max} - D_{min}}{D_{max} + D_{min}} = 1 - \frac{D_{min}}{\overline{D}}, \quad (3)$$

where D_{max} and D_{min} are the maximum and minimum of $D(\theta)$, respectively, and ϕ denotes the angle of an eigenvector to the reference direction (x-axis for convenience). Therefore, the 2D diffusion could be fully described by either the diffusion tensor $\boldsymbol{D}$ or the expression of $D(\theta)$. $D(\theta)$ acts like a correction to the average $\overline{D}$, where $0 \leq e \leq 1$ restricts the strength of the correction. For example, if e equals 0.5, we know that D_{max} equals $\overline{D} + 0.5\overline{D}$ and D_{min} equals $\overline{D} - 0.5\overline{D}$, respectively. If e equals 1, the rank of $\boldsymbol{D}$ is reduced to 1, then the 2D diffusion has degenerated into 1D diffusion. An intuitive look to the "shape" of $D(\theta)$ can be found in the polar coordinates system seen in **Fig. 2,** in which the anisotropy factor is 0.5.

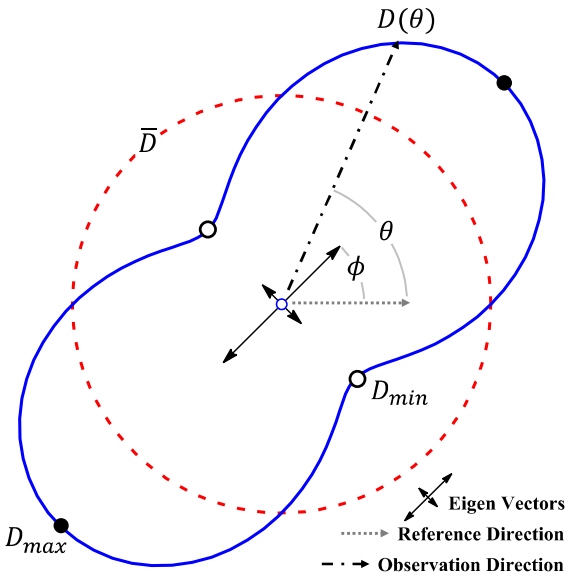

Fig. 2. Diffusivities on the surface as a function of angle to the reference direction in polar coordinates. Distance from any point on the solid blue line, $D(\theta)$, to the center is proportional to the real diffusivity at a given temperature from the observation direction (dash-dot arrow). The red dashed line represents the average diffusivity. The eigenvectors with solid double-head arrows always point to the extrema of $D(\theta)$, where θ is the angle between the observation and reference direction (gray dotted arrow), and ϕ is the angle between the eigen and reference direction.

For numerical simulations, we use trajectories from KMC to fit the components of the diffusion tensor (D_{xx}, D_{yy}, and D_{xy}) at different temperatures for point defects on the tungsten surfaces. One could calculate the diffusion tensor statistically by

$$D_{xy} = \frac{\langle \Delta x \Delta y \rangle}{2\tau}, \tag{4}$$

where Δ denotes the displacement of particles during time τ. For complex defects with finite trajectories, the drift-correction method [91-93] to reduce the computational costs. As a function of temperature, the components of diffusion tensor can be expressed in the Arrhenius form, as well as,

$$D(T) = D_0 \cdot \mathrm{e}^{-\frac{E}{k_B T}}, \tag{5}$$

where E is an effective barrier throughout all the migration paths, and D_0 is a pre-exponential factor. In the description of the diffusion tensor, we have at most two extrema (eigen) values in $D(\theta)$ for a single point defect on surfaces, D_{max} and D_{min} (**Fig. 2**). Thus, we can express the anisotropy factor using Eq. (3), at a different temperature as

$$e = \tanh\frac{1}{2}\left(\ln\frac{D_{0_{max}}}{D_{0_{min}}} - \frac{E_{max}-E_{min}}{k_B T}\right), \tag{6}$$

where $D_{0_{max}}$ and E_{max} ($D_{0_{min}}$ and E_{min}) represent the pre-exponential factor and the effective barrier along the direction of the maximum (minimum) diffusivity.

III. RESULTS AND DISCUSSION

A. Point Defect Migration Paths and Corresponding Energy Barriers

1. W (100) Surface

We have identified three mechanisms of a single adatom migration on the W (100) surface (Fig. 3), wherein the atomistic configurations are displayed following initial state (IS), transition state (TS), metastable state (MS) if exists, and final state (FS). The three mechanisms obtained by DFT are split into six paths for the reconstructed (100) surface with a mirror symmetry about the [110] direction. The adatom directly hops from the IS to its 1NN site on the (100) surface, named as path_H for hopping. H1 and H2 are for the adatom hopping over the long and short bridge, respectively, because of the reconstruction. Path_E represents a mechanism involving the exchange of atoms, where the adatom moves into the first layer beneath the surface, resulting in a <110> dumbbell-like saddle point structure, then the adatom pushes another atom out of the first layer onto the (100) surface. The dumbbell-like structures that lie along or perpendicular to the mirror axis are marked E1 and E2, respectively. In addition, the adatom may also form a <100> dumbbell-like saddle point structure via Path_R, representing rotated exchange. Similarly, R1 and R2 are for the adatom moving across the long and short bridge, respectively.

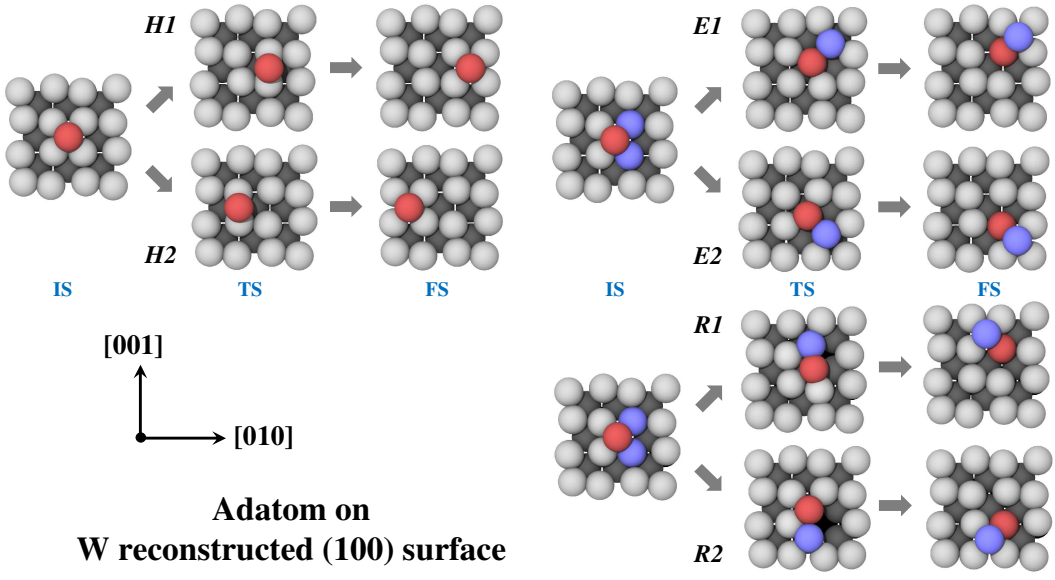

Fig. 3. Adatom migration paths on the reconstructed W (100) surface. The images follow IS, TS,

and FS from left to right. The colored atoms represent the ones with major displacements in the migration process, and the gray color from light to dark represents the depth of each layer of atoms.

Four mechanisms of a vacancy migration on the W (100) surface are found (**Fig. 4**). Three mechanisms (Path_H, Path_E, and Path_R) are similar to those of an adatom. The saddle point configuration of a vacancy in Path_R given by DFT, however, is considered as metastable states using the three interatomic potentials. We also identify an additional path, marked as Path_D for double-hopping, wherein the displacements involving two hopping atoms along the direction in Path_H. The Path_D for a vacancy is unique and not split by the reconstruction, since the two involved atoms always belong to the short or long bridge independent of hopping directions.

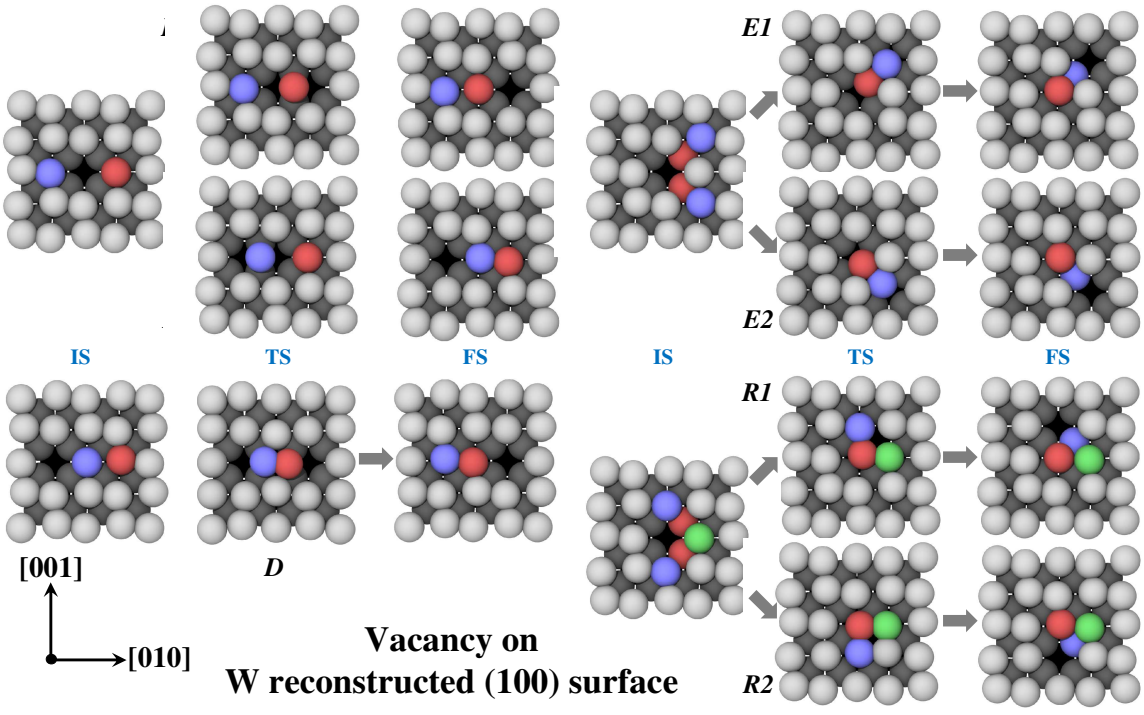

Fig. 4. Vacancy migration paths on the reconstructed W (100) surface.

The MEBs of different paths on the (100) surface are presented in **Fig. 5.** We find all potentials used in this work yield essentially the same trend. The exchange mechanism (Path_E1,2) has the

lowest MEBs for both adatoms and vacancies. MEBs of Path_H and Path_R depend on interatomic potentials, but are higher than those of Path_E, while Path_D has the highest MEBs using both interatomic potentials and DFT. The reconstruction of the W (100) surface leads to a barrier change in different directions for the same mechanism, which would lead to anisotropic diffusion. For instance, the MEB of Path_E1 for an adatom is slightly lower than that of Path_E2, whose atoms migrate along [011] and $[01\bar{1}]$, respectively, leading to enhanced jumping frequencies of defects moving along [011] at a given temperature. To obtain an accurate description of defect dynamics, all mechanisms for the W (100) surface with split paths are considered in the KMC simulations.

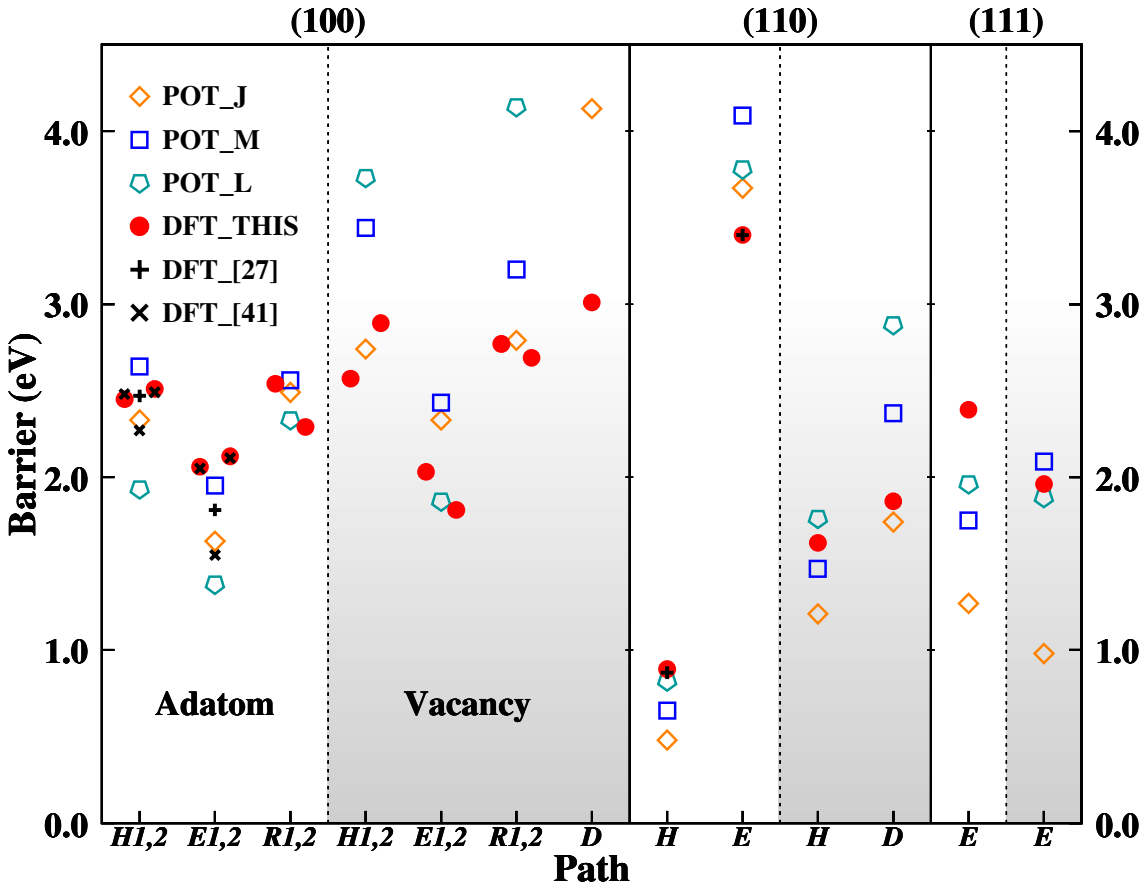

Fig. 5. Barriers of point defects migration on W surfaces obtained using different interatomic potentials and DFT. The paths are sorted by surface orientation, then defect type. Barriers from POT_J, POT_M, and POT_L are represented using a diamond, pentagon, and square, respectively. The filled circles in red representing the DFT results on the W (100) surface are seated to the left or right of the other points for the same mechanism, in which the left or right one represents the first or

second path induced by the surface reconstruction, respectively, e.g., the left representing H1 and the right representing H2. The values of '+' are taken from [27] and 'x' from [41]. The barriers of migration Path_D for a vacancy on the W (100) surface using POT_M and POT_L are 5.24 eV and 6.23 eV, respectively, which are not shown in the figure.

2. W (110) Surface

Two migration mechanisms of each point defect on the W (110) surface are presented in **Fig. 6**. The values of MEBs from these potentials show a consistent trend—the hopping mechanisms for both adatom and vacancy have the lowest MEB on this surface. Moreover, both Path_H and Path_E for an adatom agree with the DFT work by Chen et al. [27]. Chen et al. also reported a W (110) surface crowdion-crowdion (CC) mechanism with a low MEB of 0.11 eV. However, the formation energy of the crowdion is significantly higher (up to 4 eV [27]) than that of an adatom, so we do not consider the CC mechanism in KMC simulations.

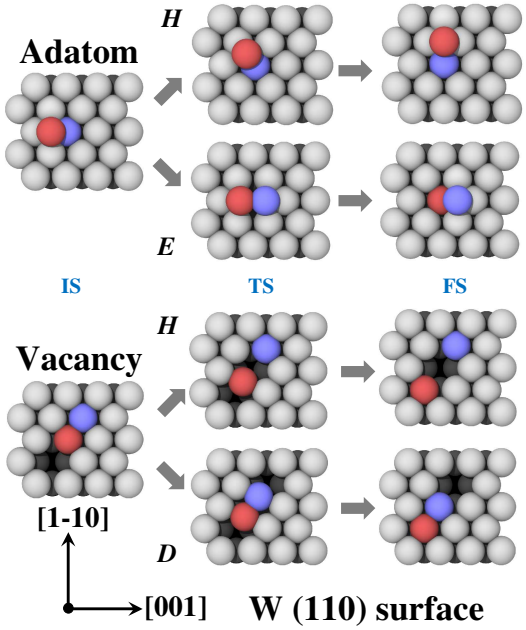

Fig. 6. Migration paths on the W (110) surface.

3. W (111) Surface

Only one migration mechanism (Path_E) on the W (111) surface is identified (**Fig. 6)** for each type of defect**.** The diffusion distance of the 1NN site for an adatom on the W (111) surface is $\sqrt{2}\ a$. No direct hopping mechanism is found in SEAKMC searches. The vacancy displays the same behavior that the neighbor atom cannot hop directly to its neighbor site.

Despite a nearly flat energy curve, both POT_M and POT_J show an MS for an adatom in the middle of Path_E. This is further verified by the DFT calculations. Path_E for a vacancy is similar to that of an adatom, but different potentials yield different metastable configurations. Unlike the paths on the other surfaces, one of the three nearest neighbor atoms (red) of the vacancy moves toward the original vacancy position first, then drags the other two neighbor atoms (green and blue) toward the vacancy position. The three colored atoms are formed into a triangular shape, which is also seen as a vacancy in the second layer at the original position of the red atom. Due to the 3-fold rotational symmetry, the metastable state could exist and have a lower formation energy than that of an adatom. The metastable states of point defects on the W (111) surface are considered in KMC simulations, where the MEBs from the metastable state to the ground state, via DFT, are 0.68 and 0.83 eV for an adatom and a vacancy, respectively.

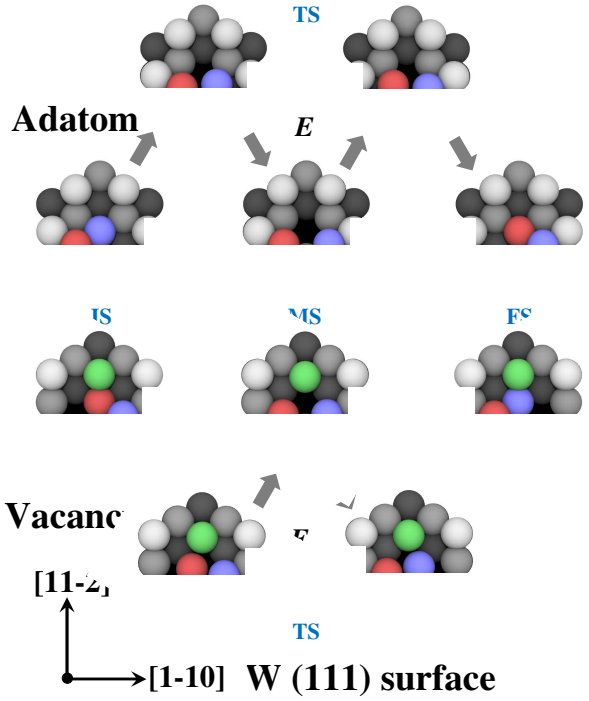

Fig. 7. Migration paths on the W (111) surface.

4. Comparison of Point Defects Migration

The MEBs of point defects on the three surfaces are compared and given in **Fig. 5 and Table 2**. The MEBs of adatoms migration on the (110) and reconstructed (100) surfaces are consistent with other DFT works [27,41]. The lowest MEB among all the adatom mechanisms is 0.89 eV by DFT of Path_H on the W (110) surface, consistent with other works [21,25,27]. However, the highest barrier of a self-interstitial atom (SIA) in bulk tungsten, reported both experimentally and theoretically, is no more than 0.1 eV (**Table 1**). Note that the configuration of an adatom is quite different from that of the SIAs. In bcc tungsten, the <111> SIA is the most stable configuration with a ~9 eV formation energy and large local strain [94]. Similarly, the MEB of CC mechanism by Chen [27] is as small as the SIA with a high formation energy up to ~4 eV. Moreover, SIA migration in bulk depends on the displacement of the crowdion configuration, and the local atoms themselves do not move a long distance. However, adatoms can directly jump between two adjacent sites on both the (100) and (110) surfaces, which might lead to the motion of impurities, e.g., isotopes and transmutation elements of tungsten [95].

For the hopping mechanism, the lowest MEB of a vacancy on the W surfaces (1.62 eV) is close to those in bulk (1.5, 1.78 eV, Table 1), which is different from the results that the MEB of a vacancy on W(001) surface is significantly smaller than bulk value by Wen et al. [33] using their interatomic potentials. These indicate the limitation of interatomic potentials applied to the surface defects calculations. In addition, the MEBs of adatoms and vacancies on surfaces are closer to each other from our DFT calculations, especially on the reconstructed (100) surface.

Table 2. Barriers of point defects migration on W surfaces using DFT. Barriers of metastable state found are marked by *.

Surface Defect	Mechanism	Barrier (eV)
(100) Adatom	H1	2.45
	H2	2.51
	E1	2.06
	E2	2.12
	R1	2.54
	R2	2.29
(100) Vacancy	H1	2.57
	H2	2.89
	E1	2.03
	E2	1.81
	R1	2.77
	R2	2.69
	D	3.01
(110) Adatom	H	0.89
	E	3.40
(110) Vacancy	H	1.62
	D	1.86
(111) Adatom	E	2.39, 0.68 *

(111) Vacancy	E	1.96, 0.83 *	

B. Diffusivity and Diffusion Anisotropy

1. W (100) Surface

The diffusivities of an adatom and a vacancy on the reconstructed (100) surface are shown in **Fig. 8**. Both defects exhibit highly anisotropic diffusion due to the reconstruction of the (100) surface. The anisotropy of a vacancy is more significant than that of an adatom at all temperatures due to a large difference in the MEBs of the same mechanism. At low temperatures, the diffusion paths of an adatom and a vacancy are always perpendicular to each other due to the tendency of the defects to migrate almost along the minimal barrier paths at low temperatures. The effective barriers for an adatom are 2.06 and 2.13 eV for the eigen directions $[011]$ and $[0\bar{1}1]$, respectively, which are almost the same as Path_E1 (2.06 eV) and E2 (2.12 eV). This is because these two paths of exchange mechanism have the lowest barriers among all the mechanisms for an adatom on the reconstructed (100) surface. Similarly, the effective barriers and eigen directions of a vacancy are dominated by Path_E1 and E2. The rest mechanisms with higher barriers contribute less either to the eigen directions or the effective barriers, which is attributed to the exponential form of jump rates expressed by the Arrhenius equation. However, due to the recovery of an ideal surface at high temperatures [83], the difference in barriers between the split paths disappears, resulting in less and less anisotropic diffusion behavior. The change of barrier difference is not considered in KMC, the anisotropic diffusion is also weakened because of the less sensitivity of diffusivities to the energy difference at high temperatures.

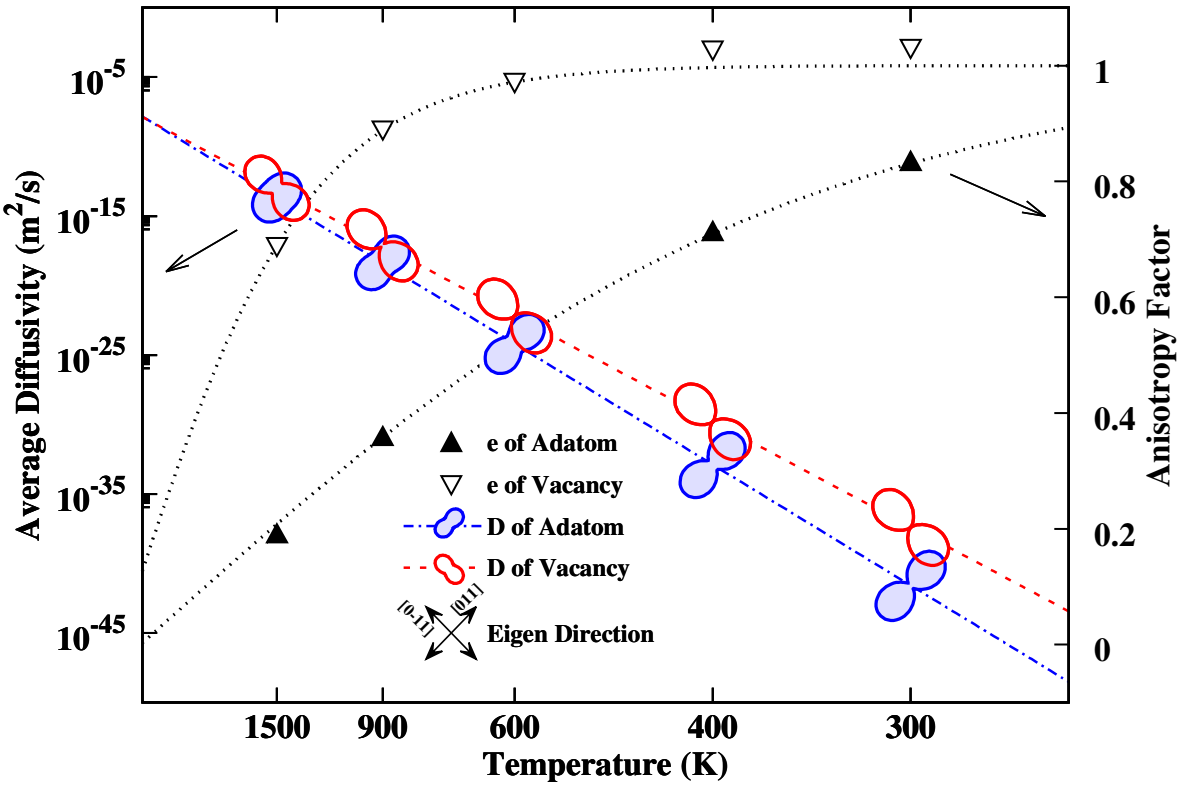

Fig. 8. Diffusivities and anisotropy factors of an adatom and a vacancy on the reconstructed W (100) surface at different temperatures. The anisotropy factors of adatom and vacancy are represented using filled and empty triangles, respectively. The centers of the peanut-like shapes represent the average diffusivities at certain temperatures, whose shapes describe the anisotropy of the diffusion tensor expressed in Fig. 2.

2. W (110) Surface

The diffusivities of an adatom and a vacancy on the W (110) surface are shown in **Fig. 9**. The average diffusivities of an adatom are higher than those of a vacancy at a given temperature because the minimal MEB of an adatom is lower than that of a vacancy. The anisotropy does not change with temperature, and anisotropy factors of both defects are 1/3, agreeing with the theoretical value. This could be attributed to that the paths and barriers on (110) surface have D_2 group symmetry, which yields that the summation of the MSD reaches a maximum projected to the $[1\bar{1}0]$ direction and a minimum to the $[001]$ direction. The ratios of the two extrema of diffusivities are independent of

temperature, derived from Eq. (6), which could be observed far above the room temperature if the structural symmetry of the surface is not broken. Notably, the diffusivities of point defects as functions of direction and temperature always follow the same symmetry as the diffusion tensor, D_2 group theoretically (Fig. 2). Thus, we predict that anisotropic morphologies exist on a wide range of surfaces not limited to the W (110) surface, e.g., W (211).

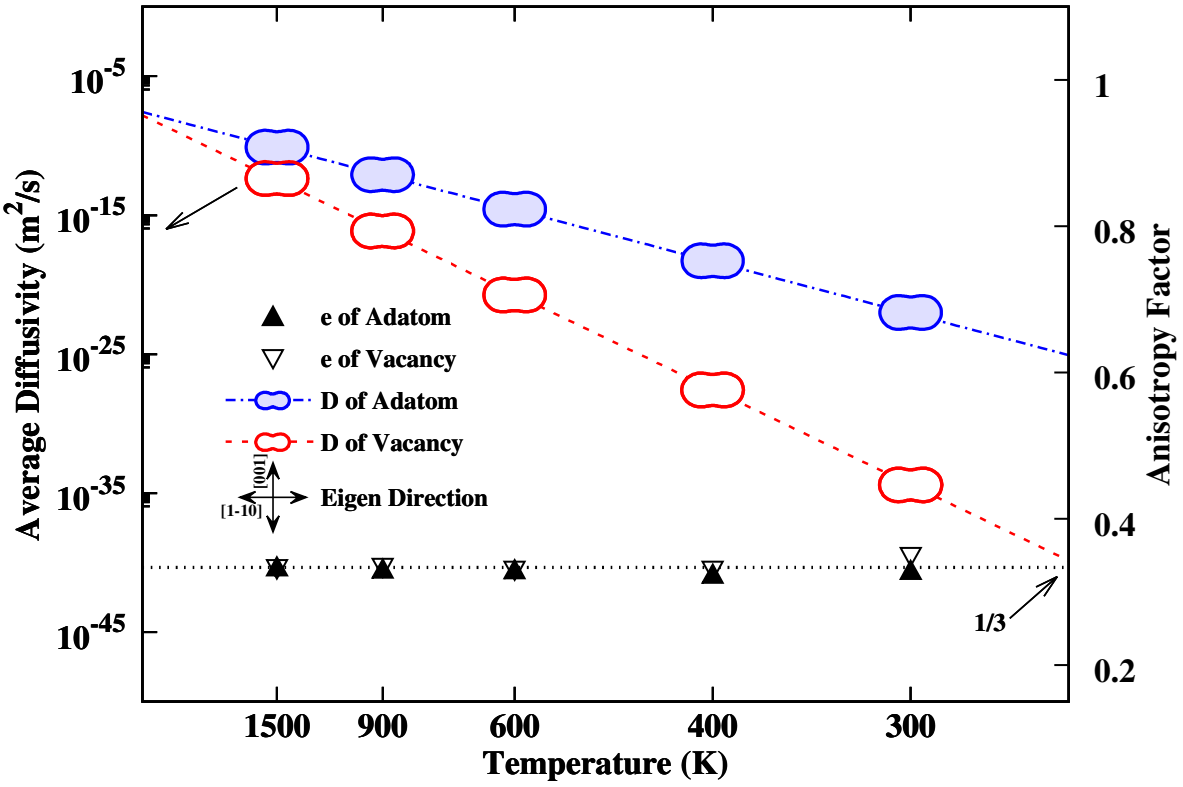

Fig. 9. Diffusivities and anisotropy factors of adatom and vacancy on the W (110) surface at different temperatures.

3. W (111) Surface

The diffusivities of defects on the W (111) surface are shown in **Fig. 10**. The adatom moves slower than a vacancy on this surface based on the MEBs by DFT, and both defects have a statistically near-isotropic diffusion tensor. All paths associated with point defect migration on the perfect (111) surface have a 3-fold rotational symmetry (**Fig. 1 and Fig. 7**), which would theoretically yield

isotropic diffusion trajectories since the summation of the projections of all MSD onto any direction are always equal. However, triangular structures are found on the W (111) surface after H isotope irradiation [10] and are also induced by sulfur overlayers [39]. These anisotropic morphologies share the same 3-fold rotational symmetry as the W (111) surface itself, and are assumed to be caused by the impurity effects, e.g. the interaction between defects and impurities.

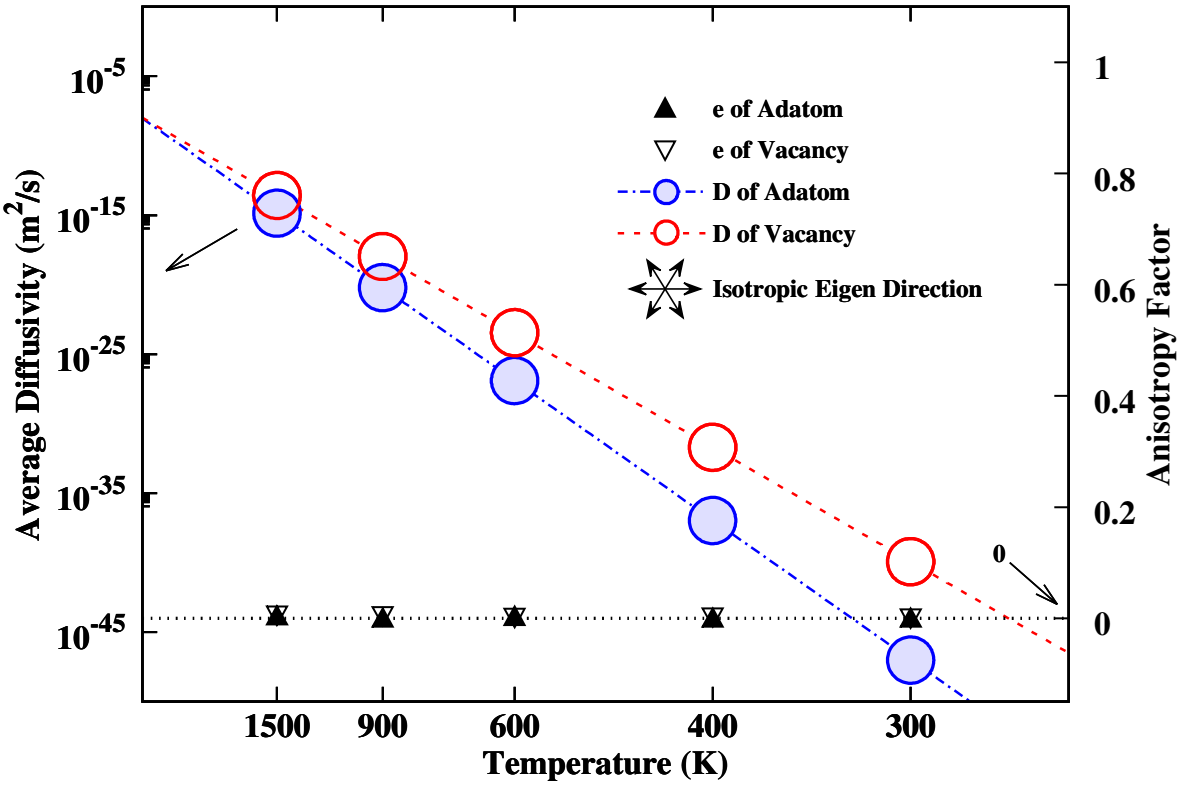

Fig. 10. Diffusivities and anisotropy factors of adatom and vacancy on the W (111) surface at different temperatures.

C. Generalized theoretical understanding of diffusion anisotropy

The diffusivities with anisotropy factors could be calculated in a more generalized manner by summing all the jump rates weighted by their jump distances and directions,

$$D(\theta) \propto \sum L_i^2 R_i \cos^2(\alpha_i - \theta), \quad (7)$$

where α_i is the angle of the i[th] path to the reference direction, L_i is the corresponding jump distance, and R_i has been expressed in Eq. (1). Then, the anisotropy factors at a given temperature could be calculated, theoretically by,

$$e = \frac{\sqrt{\sum_{i,j=1}^{n} L_i^2 L_j^2 R_i R_j \cos(2(\alpha_i - \alpha_j))}}{\sum_{i=1}^{n} L_i^2 R_i}, \tag{8}$$

and the corresponding eigen directions by,

$$\phi = \frac{1}{2}\text{acot}\frac{\sum_{i=1}^{n} L_i^2 R_i cos2\alpha_i}{\sum_{i=1}^{n} L_i^2 R_i sin2\alpha_i}, \tag{9}$$

Particularly, for the W (110) surface, at a given temperature, all the L_i and R_i are equal. The angle between migration paths is $2\text{acos}\sqrt{\frac{2}{3}}$, independent of temperature, which leads to an anisotropy factor as 1/3. In comparison, for the W (111) surface, with identical paths and barriers, the anisotropy factor is always 0, because the angle between migration paths is $\frac{\pi}{3}$. The anisotropy factor for the perfect W (100) should be 0, as well, for the 4-fold rotational symmetry of the migration mechanisms. However, the reconstruction splits the paths by different barriers along with perpendicular directions, so the R_i and R_j are no longer equal, which leads to the anisotropy factor decreasing when the temperature increases. The above analysis is consistent with the diffusivities calculated by our KMC simulations.

More generally, based on Eqs. (1), (8), and (9), we could identify four types of anisotropic diffusions of point defects on surfaces that can be used for predictions on diffusion anisotropy on any surfaces, if ignoring any temperature-dependent reconstructions of surfaces. These are: (I) isotropic diffusion, e.g., identical mechanisms with 3,4, and 6-fold rotational symmetry; (II) a fixed diffusion anisotropy for all temperatures, e.g., identical mechanisms with 2-fold rotational symmetry; (III) a decreasing diffusion anisotropy factor when temperature increases, e.g., mechanisms with equal diffusion distance but different barriers; and (IV) an initial decrease in anisotropy to isotropic diffusion when the temperature increases to a critical temperature (CT), followed by a subsequent increase of the anisotropy factor as the temperature further increases, during which the preferred migration direction changes after the CT.

Type IV would be found on surfaces with the following features: (i) one of the migration

mechanisms has a higher MEB than others', and (ii) the product of ν and L^2 is larger than others'. For instance, as the mechanisms given in [96], the adatom could diffuse along or across channels on the W(211) surface (directions of $[\bar{1}11]$ or $[01\bar{1}]$), with MEBs of 0.73 and 0.29 eV, and jump distances of $\sqrt{3}\ a$ and $2\sqrt{2}\ a$, respectively. The attempt frequency of direction $[\bar{1}11]$ is 10^5 times higher than that of the direction $[01\bar{1}]$. Based on the above parameters, we predict that the anisotropy factor falls from 1 to 0 as the temperature rises from 0 K to CT (calculated to be ~732 K). This is because the adatom prefers to move along $[01\bar{1}]$ at temperatures below CT with a lower MEB than that of the other direction. At the CT, the diffusion of an adatom is isotropic, because of equal diffusivities of both directions. Then the anisotropy factor gradually rises from 0 to 0.99 after the temperature passes CT, since the adatom moves along the $[\bar{1}11]$ direction has a higher attempt frequency than that of the other paths and the differences in MEBs are weakened at high temperatures.

IV. SUMMARY

We have performed systematic investigations of point defect dynamics on tungsten surfaces using both interatomic potentials and DFT in combination with KMC and have identified key mechanisms on several experimentally studied surfaces. On the W (100) surface, three migration mechanisms for an adatom and four mechanisms for a vacancy are found, including anisotropic migration paths caused by the surface reconstruction. In comparison, on the (110) and (111) surfaces, two and one mechanism(s) are identified for each point defect, respectively. The MEBs of the (100) surface defects are close to each other, but the values and directions are anisotropic for the same mechanism due to the reconstruction. The MEBs of the (110) surface defects are the lowest among all the mechanisms of the three surfaces, exhibiting D_2 group symmetry caused by the surface geometry. The MEBs of defects on the (111) surface have 3-fold rotational symmetry, and metastable states between two stable sites on the surface exist for both an adatom and a vacancy. The MEBs of the adatom are comparable to those of a vacancy on all three surfaces, which are much higher than the barrier of SIAs in bulk tungsten. The trends generated using different interatomic potentials and DFT are generally consistent with each other.

The diffusivities of an adatom and a vacancy on the three surfaces at different temperatures are obtained using KMC including the identified mechanisms, and the diffusion tensor is introduced to analyze the diffusion anisotropy. The average diffusivities of a vacancy on the reconstructed (100) surface are slightly higher than those of an adatom, and its diffusion tensors are more anisotropic than the adatoms'. The anisotropy factors of defects on the reconstructed (100) surface are decreased when the temperature is increased. Point defects on the (110) surface have the highest diffusivities among the three surfaces and keep a fixed anisotropy factor (1/3) independent of temperature. Isotropic diffusion of point defects is found on the (111) surface, where the diffusivity of an adatom is the lowest among all different cases on the three surfaces. In addition, we theoretically categorize four types of anisotropic diffusion, and conditions for each type of them are discussed.

These simulations provide defect transport properties of point defects on tungsten surfaces, which will be fundamental input parameters for larger-scale simulations, e.g., object KMC and mean-field rate theory. Further investigations of surface defects migration coupled with impurities under different irradiation conditions may provide useful insights to the development of a fundamental understanding

of surface blistering, fuzz formation, and the sputtering yield change of tungsten.

Acknowledgments

J. H., S. J., and G. L. acknowledge the support by the National Natural Science Foundation of China (Grant No. 11675009 and 51720105006). J. H. would like to thank the China Scholarship Council (CSC No. 201806020163) for supporting a visiting student at the University of Tennessee Knoxville (UTK). H. X. acknowledges the support of the grant DE-SC0019151 funded by the U.S. Department of Energy, Office of Science. The authors also acknowledge the computing resources of the UTK Advanced Computing Facility.

Data Availability

The raw/processed data required to reproduce these findings cannot be shared at this time as the data also forms part of an ongoing study.

References

[1] M. Shimada, A. E. Costley, G. Federici, K. Ioki, A. S. Kukushkin, V. Mukhovatov, A. Polevoi, and M. Sugihara, J Nucl Mater **337-339**, 808 (2005).

[2] D. Stork and S. J. Zinkle, Nuclear Fusion **57**, 092001 (2017).

[3] M. Rieth *et al.*, J Nucl Mater **432**, 482 (2013).

[4] V. K. Alimov and J. Roth, Physica Scripta **T128**, 6 (2007).

[5] T. Tanabe, Physica Scripta **T159**, 014044 (2014).

[6] M. J. Baldwin and R. P. Doerner, Nuclear Fusion **48**, 035001 (2008).

[7] M. J. Baldwin, T. C. Lynch, R. P. Doerner, and J. H. Yu, J Nucl Mater **415**, 104 (2011).

[8] M. R. Gilbert and J. C. Sublet, Nuclear Fusion **51** (2011).

[9] X. Hu, T. Koyanagi, M. Fukuda, N. A. P. K. Kumar, L. L. Snead, B. D. Wirth, and Y. Katoh, J Nucl Mater **480**, 235 (2016).

[10] H. Y. Xu, Y. B. Zhang, Y. Yuan, B. Q. Fu, A. Godfrey, G. De Temmerman, W. Liu, and X. Huang, J Nucl Mater **443**, 452 (2013).

[11] F. W. Meyer, H. Hijazi, M. E. Bannister, K. A. Unocic, L. M. Garrison, and C. M. Parish, Physica Scripta **T167**, 014019 (2016).

[12] Y. Z. Jia, W. Liu, B. Xu, G. N. Luo, S. L. Qu, T. W. Morgan, and G. De Temmerman, J Nucl Mater **477**, 165 (2016).

[13] C. M. Parish, H. Hijazi, H. M. Meyer, and F. W. Meyer, Acta Mater **62**, 173 (2014).

[14] N. Ohno, Y. Hirahata, M. Yamagiwa, S. Kajita, M. Takagi, N. Yoshida, R. Yoshihara, T. Tokunaga, and M. Tokitani, J Nucl Mater **438**, S879 (2013).

[15] C. M. Parish, K. Wang, R. P. Doerner, and M. J. Baldwin, Scripta Mater **127**, 132 (2017).

[16] A. V. Barashev, H. Xu, and R. E. Stoller, J Nucl Mater **454**, 421 (2014).

[17] H. Gnaser and H. Gnaser, *Low-energy ion irradiation of solid surfaces* (Springer, 1999), Vol. 146.

[18] J. Jussila, M.Sc., UNIVERSITY OF HELSINKI, 2019.

[19] K. Nordlund *et al.*, J Nucl Mater **512**, 450 (2018).

[20] G. Ehrlich and F. G. Hudda, The Journal of Chemical Physics **44**, 1039 (1966).

[21] M. J. Parsley, Diploma of Membership of the Imperial College of Science and

Technology, Imperial College, 1969.

[22] D. Bassett and M. Parsley, Journal of Physics D: Applied Physics **3**, 707 (1970).

[23] D. Cowel Senft and G. Ehrlich, Physical review letters **74**, 0 (1995).

[24] P. Wynblatt and N. A. Gjostein, Surf Sci **22**, 125 (1970).

[25] D. Chen, W. Hu, J. Yang, H. Deng, L. Sun, and F. Gao, European Physical Journal B **68**, 479 (2009).

[26] R. Fijak, L. Jurczyszyn, and G. Antczak, Surf Sci **605**, 282 (2011).

[27] Z. Chen and N. Ghoniem, Physical Review B **88**, 1 (2013).

[28] P. Wynblatt and N. A. Gjostein, Surf Sci **22**, 125 (1970).

[29] W. Xu and J. B. Adams, Surf Sci **319**, 58 (1994).

[30] G. Antczak and G. Ehrlich, Physical Review Letters **92**, 1 (2004).

[31] G. Antczak, Physical Review B **73**, 033406 (2006).

[32] V. Jansson, A. Kyritsakis, S. Vigonski, E. Baibuz, V. Zadin, A. Aabloo, and F. Djurabekova, Modelling and Simulation in Materials Science and Engineering (2020).

[33] Y. N. Wen, J. M. Zhang, and K. W. Xu, Colloids and Surfaces A: Physicochemical and Engineering Aspects **304**, 67 (2007).

[34] G. Duan *et al.*, Nuclear Instruments and Methods in Physics Research, Section B: Beam Interactions with Materials and Atoms **414**, 29 (2018).

[35] M. K. Debe and D. A. King, Physical Review Letters **39**, 708 (1977).

[36] M. K. Debe and D. A. King, Journal of Physics C: Solid State Physics **10**, L303 (1977).

[37] R. D. Kolasinski, K. D. Hammond, J. A. Whaley, D. A. Buchenauer, and B. D. Wirth, J Nucl Mater **463**, 1053 (2015).

[38] A. Yoshimori, Progress of Theoretical Physics Supplement **106**, 433 (1991).

[39] R. a. Barker, The Journal of Chemical Physics **74**, 1442 (1981).

[40] C. H. Nien and T. E. Madey, Surf Sci **433**, 254 (1999).

[41] T. Olewicz, G. Antczak, L. Jurczyszyn, J. W. Lyding, and G. Ehrlich, Physical Review B **89**, 235408 (2014).

[42] G. Antczak and G. Ehrlich, Physical review letters **92**, 166105 (2004).

[43] S.-M. Oh, K. Kyuno, S. J. Koh, and G. Ehrlich, Physical Review B **66**, 233406 (2002).

[44] D. R. Bowman, R. Gomer, K. Muttalib, and M. Tringides, Surf Sci **138**, 581 (1984).

[45] L. Vitos, A. V. Ruban, H. L. Skriver, and J. Kollár, Surf Sci **411**, 186 (1998).

[46] A. I. Belyaeva, A. A. Savchenko, A. A. Galuza, and I. V. Kolenov, Probl Atom Sci Tech, 14 (2017).

[47] H. Xu, Y. N. Osetsky, and R. E. Stoller, Journal of Physics: Condensed Matter **24**, 375402 (2012).

[48] H. Xu, Y. N. Osetsky, and R. E. Stoller, Physical Review B - Condensed Matter and Materials Physics **84**, 1 (2011).

[49] A. Ervin and H. Xu, Computational Materials Science **150**, 180 (2018).

[50] G. Henkelman, B. P. Uberuaga, and H. Jónsson, The Journal of Chemical Physics **113**, 9901 (2000).

[51] G. Henkelman and H. Jónsson, The Journal of Chemical Physics **113**, 9978 (2000).

[52] E. Maras, O. Trushin, A. Stukowski, T. Ala-Nissila, and H. Jónsson, Computer Physics Communications **205**, 13 (2016).

[53] A. Nakano, Computer Physics Communications **178**, 280 (2008).

[54] M. W. Finnis and J. E. Sinclair, Philosophical Magazine A **50**, 45 (1984).

[55] G. J. Ackland and R. Thetford, Philosophical Magazine A **56**, 15 (1987).

[56] N. Juslin and B. D. Wirth, J Nucl Mater **432**, 61 (2013).

[57] J. Tersoff, Physical Review B **37**, 11 (1988).

[58] X. C. Li, X. Shu, Y. N. Liu, F. Gao, and G. H. Lu, J Nucl Mater **408**, 12 (2011).

[59] X. C. Li, X. Shu, Y. N. Liu, Y. Yu, F. Gao, and G. H. Lu, J Nucl Mater **426**, 31 (2012).

[60] M. S. Daw and M. I. Baskes, Physical Review B **29**, 6443 (1984).

[61] L.-F. Wang, X. Shu, G.-H. Lu, and F. Gao, Journal of Physics: Condensed Matter **29**, 435401 (2017).

[62] M.-C. Marinica, L. Ventelon, M. R. Gilbert, L. Proville, S. L. Dudarev, J. Marian, G. Bencteux, and F. Willaime, Journal of physics. Condensed matter : an Institute of Physics journal **25**, 395502 (2013).

[63] K. Heinola, T. Ahlgren, K. Nordlund, and J. Keinonen, Physical Review B - Condensed Matter and Materials Physics **82**, 1 (2010).

[64] Y. Oda, A. M. Ito, A. Takayama, and H. Nakamura, Plasma and Fusion Research **9**, 3 (2014).

[65] C. Kittel, *Introduction to Solid State Physics* (John Wiley and Sons, New York, 1996), 7th edn.

[66] E. Lassner and W.-D. Schubert, *Tungsten:Properties,Chemistry,Technology of the Element,Alloys,and Chemical Compounds* (Kluwer Academic, New York, 1999).

[67] J. Hao, X. Shu, S. Jin, X. Zhang, Y. Zhang, and G.-H. Lu, Nuclear Instruments and Methods in Physics Research Section B: Beam Interactions with Materials and Atoms **393**, 180 (2016).

[68] W. Tyson and W. Miller, Surf Sci **62(1)**, 267 (1977).

[69] F. R. de Boer, R. Boom, W. C. M. Mattens, A. R. Miedema, and A. K. Niessen, (1989).

[70] I. M. Neklyudov, E. V. Sadanov, G. D. Tolstolutskaja, V. A. Ksenofontov, T. I. Mazilova, and I. M. Mikhailovskij, Physical Review B - Condensed Matter and Materials Physics **78**, 1 (2008).

[71] K. D. Rasch, R. W. Siegel, and H. Schultz, Philosophical Magazine A: Physics of Condensed Matter, Structure, Defects and Mechanical Properties **41**, 91 (1980).

[72] J. Y. Park, H. C. W. Huang, R. W. Siegel, and R. W. Balluffi, Philosophical Magazine A: Physics of Condensed Matter, Structure, Defects and Mechanical Properties **48**, 397 (1983).

[73] F. Dausinger and H. Schultz, Physical Review Letters **35**, 1773 (1975).

[74] J. N. Mundy, S. T. Ockers, and L. C. Smedskjaer, Philosophical Magazine A: Physics of Condensed Matter, Structure, Defects and Mechanical Properties **56**, 851 (1987).

[75] D. F. Johnson and E. A. Carter, Journal of Materials Research **25**, 315 (2010).

[76] G. Henkelman and H. Jónsson, Journal of Chemical Physics **111**, 7010 (1999).

[77] A. Heyden, A. T. Bell, and F. J. Keil, Journal of Chemical Physics **123** (2005).

[78] S. Plimpton, Journal of Computational Physics **117**, 1 (1995).

[79] J. P. Perdew and Y. Wang, Physical Review B **45**, 1689 (1992).

[80] G. Kresse and J. Furthmüller, Physical Review B **54**, 11169 (1996).

[81] G. Kresse and J. Furthmüller, Computational Materials Science **6**, 15 (1996).

[82] G. Kresse and J. Hafner, Physical Review B **47**, 558 (1993).

[83] D. A. King, Physica Scripta **T4**, 34 (1983).

[84] J. D. Pack and H. J. Monkhorst, Physical Review B **16**, 1748 (1977).

[85] E. Wigner, T Faraday Soc **34**, 0029 (1938).

[86] H. Eyring, T Faraday Soc **34**, 0041 (1938).

[87] G. H. Vineyard, J Phys Chem Solids **3**, 121 (1957).

[88] A. BORTZ, M. KALOS, and J. LEBOWITZ, Journal of Computational Physics **17**, 10 (1975).

[89] G. Antczak and G. Ehrlich, *Surface diffusion: metals, metal atoms, and clusters* (Cambridge University Press, 2010).

[90] H. Mehrer, *Diffusion in Solids - Fundamentals, Methods, Materials, Diffusion-Controlled Processes* 2007), Springer Series in Solid-State Sciences.

[91] P. Derlet, M. Gilbert, and S. Dudarev, Physical Review B **84**, 134109 (2011).

[92] P. M. Derlet, D. Nguyen-Manh, and S. L. Dudarev, Physical Review B - Condensed Matter and Materials Physics **76**, 1 (2007).

[93] S. L. Dudarev, Comptes Rendus Physique **9**, 409 (2008).

[94] D. Nguyen-Manh, A. P. Horsfield, and S. L. Dudarev, Physical Review B - Condensed Matter and Materials Physics **73**, 4 (2006).

[95] Y. H. Li, H. B. Zhou, S. Jin, Y. Zhang, H. Deng, and G. H. Lu, Nuclear Fusion **57** (2017).

[96] D.-S. Choi and R. Gomer, Surf Sci **230**, 277 (1990).

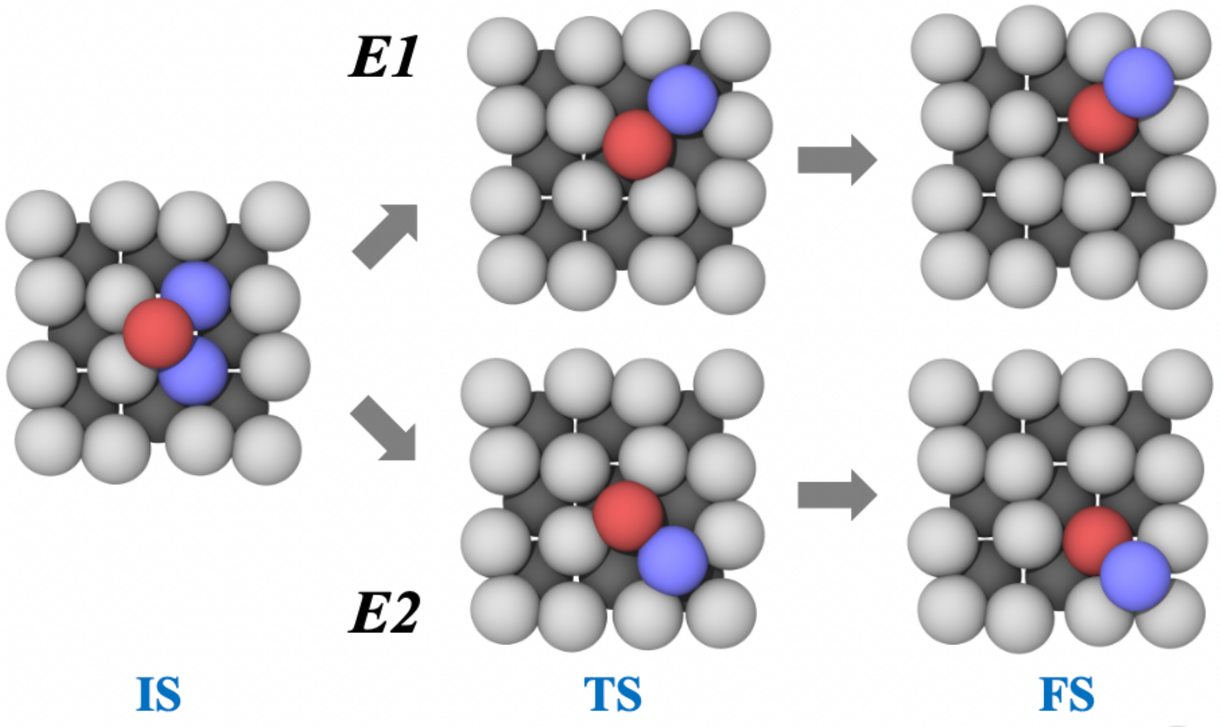

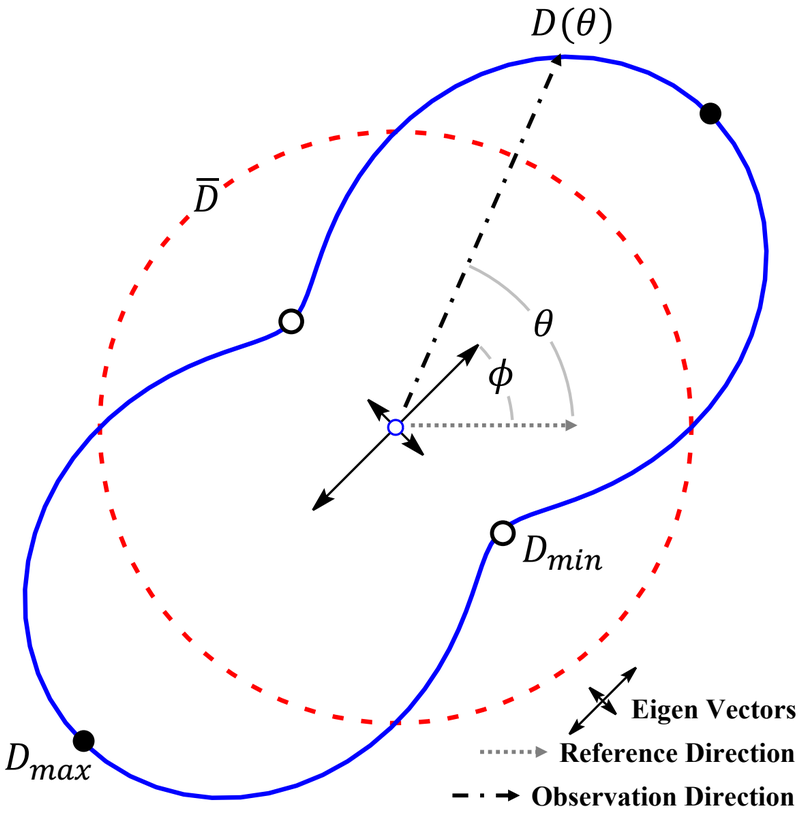

Multiple migration mechanisms → **Anisotropic diffusion on tungsten surfaces**